Chem

CellPress

Article

# Selective Surface PEGylation of UiO-66 Nanoparticles for Enhanced Stability, Cell Uptake, and pH-Responsive Drug Delivery

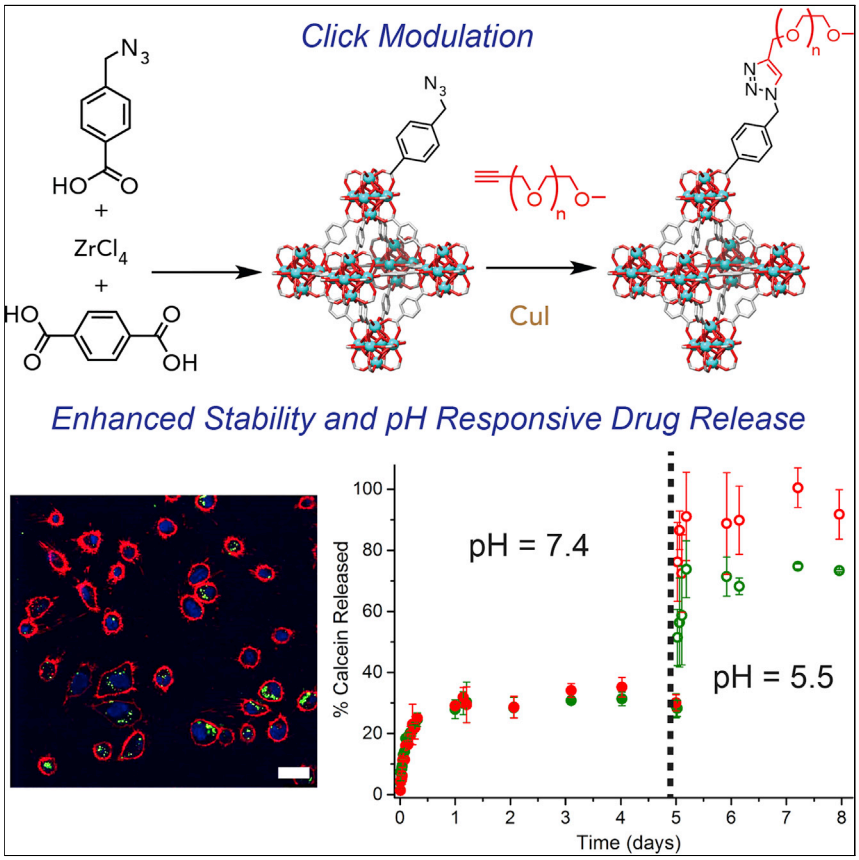


Porous nanoparticles that can store drug molecules have great potential in drug delivery, the use of nanocarriers to transport therapeutic agents around the body. Forgan and colleagues report on a method that controls the surface properties and functionality of metal-organic framework nanoparticles to enhance their stability, allow stimuli-responsive release of drug molecules, and enhance the anticancer therapeutic effect of loaded drugs by changing the route of cell uptake. Further development of these materials could enhance drug efficiencies and avoid unwanted side effects.

Isabel Abánades Lázaro, Salame Haddad, Sabrina Sacca, Claudia Orellana-Tavra, David Fairen-Jimenez, Ross S. Forgan

df334@cam.ac.uk (D.F.-J.)
ross.forgan@glasgow.ac.uk (R.S.F.)

## HIGHLIGHTS

A surface modification protocol for MOFs compatible with cargo loading is reported

PEGylated UiO-66 nanoparticles show pH-responsive cargo release

Endocytosis routes are modified by the control of MOF surface chemistry

Enhanced cytotoxicity is observed for PEGylated UiO-66 loaded with dichloroacetate

Abánades Lázaro et al., Chem 2, 561–578
April 13, 2017 
http://dx.doi.org/10.1016/j.chempr.2017.02.005

Chem

CellPress

Article

# Selective Surface PEGylation of UiO-66 Nanoparticles for Enhanced Stability, Cell Uptake, and pH-Responsive Drug Delivery

Isabel Abánades Lázaro,[1] Salame Haddad,[2] Sabrina Sacca,[1] Claudia Orellana-Tavra,[2] David Fairen-Jimenez,[2,*] and Ross S. Forgan[1,3,*]

## SUMMARY

**The high storage capacities and excellent biocompatibilities of metal-organic frameworks (MOFs) have made them emerging candidates as drug-delivery vectors. Incorporation of surface functionality is a route to enhanced properties, and here we report on a surface-modification procedure—click modulation—that controls their size and surface chemistry. The zirconium terephthalate MOF UiO-66 is (1) synthesized as ~200 nm nanoparticles coated with functionalized modulators, (2) loaded with cargo, and (3) covalently surface modified with poly(ethylene glycol) (PEG) chains through mild bioconjugate reactions. At pH 7.4, the PEG chains endow the MOF with enhanced stability toward phosphates and overcome the "burst release" phenomenon by blocking interaction with the exterior of the nanoparticles, whereas at pH 5.5, stimuli-responsive drug release is achieved. The mode of cellular internalization is also tuned by nanoparticle surface chemistry, such that PEGylated UiO-66 potentially escapes lysosomal degradation through enhanced caveolae-mediated uptake. This makes it a highly promising vector, as demonstrated for dichloroacetic-acid-loaded materials, which exhibit enhanced cytotoxicity. The versatility of the click modulation protocol will allow a wide range of MOFs to be easily surface functionalized for a number of applications.**

## INTRODUCTION

Effective cancer therapy is one of the most challenging goals for the scientific community because of the lack of tumor selectivity of most therapeutics, which can lead to toxic dose dependence, serious hepatic problems, and diverse side effects.[1–3] Thus, drug-delivery systems have become one of the most promising applications for health care.[4–6] A large number of strategies have been studied, but for application, drug-delivery systems must overcome issues surrounding bioavailability,[7,8] the uncontrollable release of drugs (usually due to carrier instability),[9–11] loading capacities,[11–13] particle size,[14–16] nanoparticle cellular internalization routes,[14,17,18] and toxicity.[19,20] The exceptional storage capacities of metal-organic frameworks (MOFs), together with their robustness and structural tailorability, have made them attractive for a wide variety of applications,[21,22] including several promising breakthroughs in biomedicine.[9,10,23–33] One of their main advantages is that their cytotoxicity and properties can be tuned by the thoughtful choice of metal and linkers.[20,34,35]

Surface modifications of drug nanocarriers are of high importance because the carrier stability, drug-release kinetics, and particle cellular internalization can be

### The Bigger Picture

Using artificial agents to deliver drugs selectively to sites of disease while protecting them from metabolism and clearance offers potential routes to new treatments. Porous metal-organic frameworks (MOFs) have emerged as potential candidates because they offer high storage capacities and easy clearance after delivery. We report on a method that controls the size and surface chemistry of MOFs and is compatible with cargo loading, showing that surface modification with biocompatible poly(ethylene glycol) chains improves stability toward phosphate and allows pH-responsive cargo release, which could enhance selectivity because cancerous cells are typically more acidic than healthy ones. Modes of cellular uptake are also altered, which could account for the enhanced cell death when polymer-coated MOFs are loaded with the anticancer drug dichloroacetic acid. Surface modification is mild and could be applied across a range of MOFs, opening up applications in selective molecular separation, blending into hybrids, and turn-on catalysis.

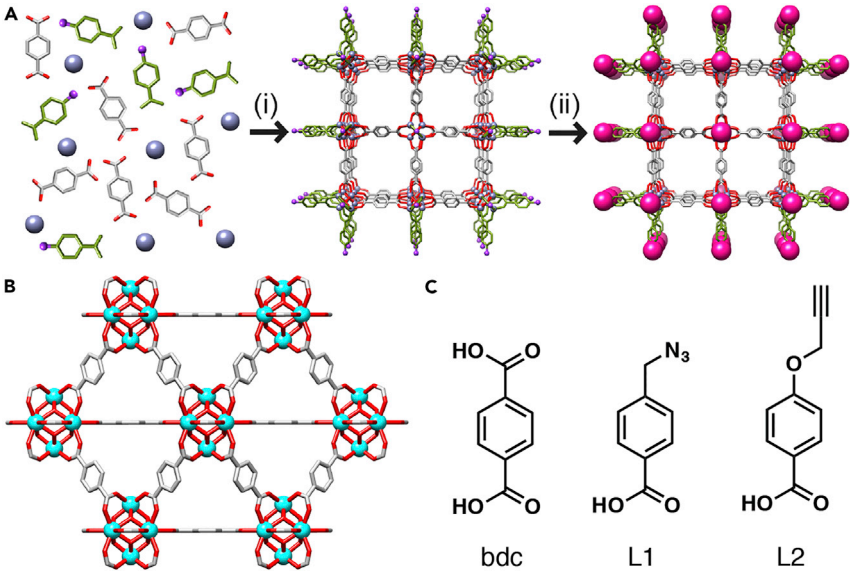


**Figure 1. Click Modulation of UiO-66 MOFs**

(A) Schematic of the "click modulation" protocol, where functionalized modulators are (i) incorporated onto MOF surfaces during synthesis and (ii) selectively chemically modified.
(B) The structure of UiO-66, which has been functionalized by click modulation.
(C) The ligand, bdc, and modulators (L1 and L2) applied in this study.

tuned.[9,18] Particle characteristics such as size, shape, and surface chemistry play key roles in determining the cellular-uptake pathways.[36–38] Although a considerable amount of work has been performed to modify the bulk structure and internal pore spaces of MOFs,[39–42] only a few studies have addressed their external surface chemistry, usually through surface-selective postsynthetic modification protocols designed for specific MOFs and surface substrates.[9,24,43–48] For example, coatings with different polymers have decreased immune system recognition and accumulation in the liver for nanoparticulate MOFs (NMOFs) and have shown promising in vitro and in vivo results in anticancer therapy.[9,24] In addition, they can be targeted to cancer cells by the attachment of different targeting units to their surface through postsynthetic modifications, avoiding non-specific distribution of the drug.[49,50]

The size and shape of NMOF particles can be tuned by the introduction of modulators—monotopic capping agents such as benzoic acid—to their syntheses.[51–55] Coordination modulation offers the prospect of decorating the external surfaces of NMOFs with desirable functionality during the synthetic process, but this remains a challenge.[56,57] Herein, we present a reproducible two-step method, which we have termed "click modulation," for the general surface modification of zirconium-based NMOFs (Figure 1A). This method introduces functionalized modulators to the NMOFs' external surfaces during the synthetic process to control particle size and subsequently transforms them in further postsynthetic modifications by using high-yielding "click" chemistry compatible with cargo-loaded NMOFs.

Incorporation of polymers onto the external surfaces of NMOFs has been suggested as a route to enhanced stability and effective application in drug delivery.[58] We have therefore used our click modulation protocol to covalently attach poly(ethylene glycol) (PEG) chains to the NMOFs' surfaces to improve their stability and drug-release kinetics and also facilitate pH-responsive release of cargo. The effect of

[1]WestCHEM School of Chemistry, University of Glasgow, Joseph Black Building, University Avenue, Glasgow G12 8QQ, UK

[2]Adsorption & Advanced Materials Laboratory, Department of Chemical Engineering & Biotechnology, University of Cambridge, Pembroke Street, Cambridge CB2 3RA, UK

[3]Lead Contact

*Correspondence: df334@cam.ac.uk (D.F.), ross.forgan@glasgow.ac.uk (R.S.F.)

http://dx.doi.org/10.1016/j.chempr.2017.02.005

postsynthetic surface modification on cancer cell endocytosis pathways was also studied,[14,38] revealing that cellular internalization routes of NMOFs can be mediated by their surface chemistry.

## RESULTS AND DISCUSSION

The zirconium MOF UiO-66 (UiO stands for Universitetet i Oslo; Figure 1B)[59] is biocompatible and has a half maximal inhibitory concentration ($IC_{50}$) of 1.50 ± 0.15 mg/mL against the HeLa cell line after 24 hr of exposure.[60] Its idealized structure, $Zr_6O_4(OH)_4(bdc)_6$, where bdc stands for 1,4-benzenedicarboxylate, has been well characterized and possesses a remarkable thermal and chemical stability in comparison with that of other MOFs.[59,61,62] UiO-66 is also known to incorporate synthetic modulators at surface and defect sites[63–65] and so was chosen for study. *p*-Azidomethylbenzoic acid (L1) and *p*-propargyloxybenzoic acid (L2) were selected as click modulators (Figure 1C) for UiO-66 synthesis because of their structural similarities to the bdc linker and the fact that, if attached to the $Zr_6$ clusters, the desired functionalities should point outward,[46] resulting in accessible reactive groups as platforms for further postsynthetic modifications on its surface.

### Synthesis and Characterization of UiO-66-L1 and UiO-66-L2

UiO-66 nanoparticles were synthesized under solvothermal conditions (Supplemental Information, Section S2) by the addition of 1, 3, or 5 equiv of the desired modulator (L1 or L2) and acetic acid (AcOH) as the co-modulator. Full characterization (Supplemental Information, Section S3) showed that the particles were highly crystalline, as confirmed by powder X-ray diffraction (PXRD) (Figure S1), and nuclear magnetic resonance (NMR) spectroscopy of acid-digested samples showed that modulator incorporation increased with the number of equivalents of modulator added to the reaction mixture (Figures S2 and S3); the estimated maximum content was 13.3 mol % of L1 (5 equiv added) in comparison with bdc and 17.1 mol % of L2 (5 equiv added). Infrared (IR) spectroscopy revealed an increase in the intensity of the azide vibration band at 2,100 $cm^{-1}$ as the number of equivalents of L1 in UiO-66-L1 syntheses increased, whereas vibration bands characteristic of C≡C triple bonds were observed for UiO-66-L2 (Figure S4). Because of these encouraging results, all subsequent syntheses utilized 5 equiv of the corresponding modulator and 7% v/v of AcOH, and these samples are designated UiO-66-L1 and UiO-66-L2. A comparison sample, UiO-66-AcOH, was prepared in a synthesis modulated only by 7% v/v AcOH.

Quantifying modulator incorporation by thermogravimetric analysis (TGA) is difficult; compared with UiO-66-AcOH, modulated samples did not lose extra mass, indicating that the modulators, which are chemically similar to the bdc linkers and whose presence was confirmed by $^1H$ NMR spectroscopy, decompose at similar temperature (Figure S8). This suggests that L1 and L2 are attached to the external surface and at defect sites of the MOF and not simply loaded in the pores. UiO-66 has been reported to be highly porous; if defect free, its Brunauer-Emmet-Teller (BET) surface area is around 1,200 $m^2\ g^{-1}$, and its pore volume is 0.5 $cm^2\ g^{-1}$.[59] To characterize the porosity of UiO-66-L1 and UiO-66-L2, we collected $N_2$ adsorption isotherms at 77 K (Figure S9). The modulated samples exhibited higher surface areas ($S_{BET}$ = 1,565 $m^2\ g^{-1}$ for UiO-66-L1 and 1,420 $m^2\ g^{-1}$ for UiO-66-L2), again suggesting that modulator incorporation induces defects rather than simply occupying and blocking pores,[57] and the pore-size distributions of the modulated samples were similar to those reported for UiO-66 (8 and 11 Å).[59]

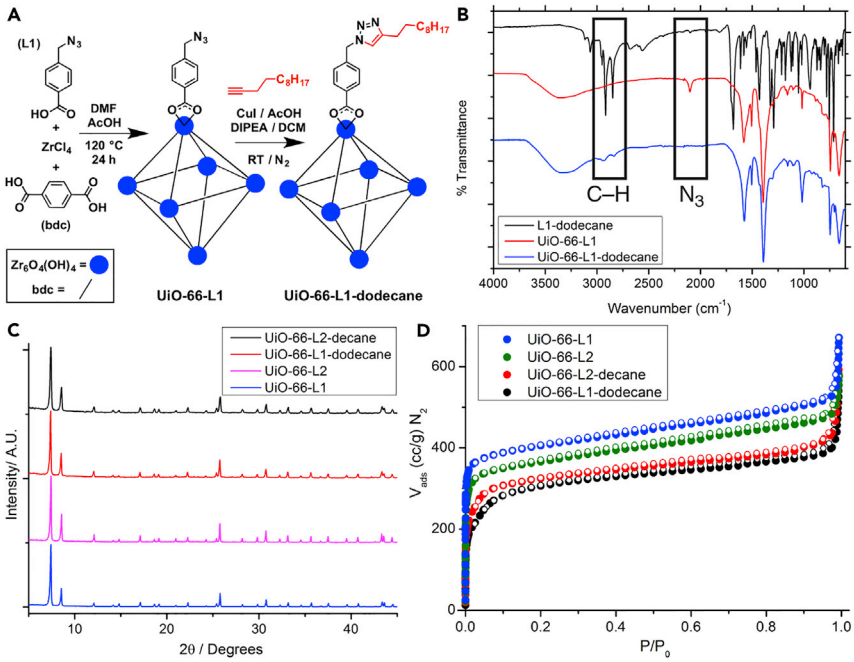


**Figure 2. Proof-of-Concept Surface Modification of UiO-66 with Alkanes**

(A) Schematic of the click modulation protocol in the preparation of UiO-66-L1-dodecane.

(B) Stacked IR spectra showing the disappearance of the azide stretch and appearance of C–H signals after the CuAAC surface reaction has taken place on UiO-66-L1.

(C) Stacked PXRD profiles of UiO-66-L1 and UiO-66-L2 before and after alkylation.

(D) $N_2$ adsorption isotherms (77 K) of the MOFs show a decrease in gravimetric uptake as additional mass is incorporated onto their surfaces. Closed symbols represent adsorption, and empty symbols represent desorption.

## Proof-of-Concept Surface Functionalization

After confirming that the functionalized modulators were incorporated into the MOF structure, we attempted postsynthetic modification by copper(I)-catalyzed azide-alkyne cycloaddition (CuAAC)[66] (Supplemental Information, Section S4). Various catalysts were tested, including CuI and a mixture of $CuSO_4$ and sodium ascorbate, resulting in loss of the sample crystallinity each time. An efficient and economic approach, using CuI and 2 equiv of both acetic acid and *N,N*-diisopropylethylamine as an in situ stabilizing ligand for Cu(I),[67] was tolerated by the MOF structure, as confirmed by PXRD (Figure S10), and allowed further functionalization of the NMOFs.

Proof-of-concept reactions using this catalyst were carried out between UiO-66-L1 and 1-dodecyne (Figure 2A), as well as between UiO-66-L2 and 1-azidodecane. $^1$H NMR spectra of acid-digested samples of UiO-66-L1-dodecane and UiO-66-L2-decane suggested significant conversions of the modulators into the respective triazole products; although the low modulator content makes analysis difficult, additional aromatic signals are present alongside peaks for the alkyl groups. Full conversion would not be expected, given that some modulators will be located at inaccessible internal defect sites rather than on the particle surface.

Fourier transform IR (FT-IR) spectra also showed the disappearance of signals for modulator azide and alkyne groups and the appearance of triazole bands and surface functionality, which compared well with spectra of authentic samples of

"clicked" modulators prepared separately in solution-phase reactions (Figure 2B), whereas high-resolution electrospray ionization mass spectrometry (HR-ESI-MS) of acid digests of the modified MOFs confirmed the presence of the triazole products. The crystallinity, as measured by PXRD (Figure 2C), and porosity (Figure 2D) of the samples after functionalization with alkyl chains were both maintained, such that surface areas were slightly lower (1,168 $m^2\ g^{-1}$ for UiO-66-L1-dodecane and 1,262 $m^2\ g^{-1}$ for UiO-66-L2-decane) that those of their precursors, UiO-66-L1 (1,565 $m^2\ g^{-1}$) and UiO-66-L2 (1,420 $m^2\ g^{-1}$). Surface functionalization with alkyl chains increases the mass of the particles, and so a decrease in gravimetric surface area is expected.[68] These decreases correlate well with the new mass-loss features observed in TGA profiles of UiO-66-L1-dodecane and UiO-66-L2-decane (10.1% and 10.0% w/w, respectively), which correspond to decomposition of the surface alkyl chains of the functionalized materials (Figures S12 and S13).

Scanning electron microscopy (SEM) showed that UiO-66-L1 forms well-defined nanoparticles around 100–200 nm in size (Figure S6) in a manner similar to a recently reported modulated synthesis of a related zirconium fumarate MOF.[69,70] In contrast, UiO-66-L2 has a larger particle size, around 400–600 nm (Figure S7), suggesting that click modulation can be used to control nanoparticle size as well as surface chemistry. Because the UiO-66-L1 nanoparticles have the appropriate size for drug-delivery applications,[16] we decided to continue our research toward surface functionalization of UiO-66-L1 for drug delivery. Specifically, PEG chains were chosen because they present an amphiphilic behavior that resembles that of human cellular membranes,[71] whereby the flexible and rapidly changing structure of the PEG hinders the immune system in the modeling of antibodies around it.[72]

The monomethyl ethers of PEG550 (average $M_n$ = 550) and PEG2000 (average $M_n$ = 2,000) were alkylated with propargyl units and used for conjugation with the azide-functionalized UiO-66-L1 under the previously determined Cu(I)-catalyzed conditions (Supplemental Information, Section S4). Full $^1$H NMR spectroscopic analysis of the acid-digested products, UiO-66-L1-PEG550 and UiO-66-L1-PEG2000, is difficult because of the intensity of the polymer signals. However, a control experiment—stirring PEG2000-propargyl or PEG550-propargyl with UiO-66-L1 but without catalyst—revealed that, without Cu(I) catalyst, no polymer was present in the sample at all, confirming that covalent linkage is required for the PEG to remain attached to the MOF.

TGA profiles of UiO-66-L1-PEG550 and UiO-66-L1-PEG2000 (Figure 3A) showed extra mass losses (21.7% and 23.1% w/w, respectively) at temperatures corresponding to those reported for PEG in the literature,[73] whereas no extra mass losses were found in the control samples. HR-ESI-MS of digested UiO-66-L1-PEG550 (Figure 3B) confirmed that the click reaction between UiO-66-L1 and PEG550-propargyl had taken place, and although derivatives of the larger PEG2000 species did not ionize under the available conditions, functional-group conversion was observed by IR spectroscopy (Figure S16).

PXRD confirmed that the PEGylated NMOFs retained their crystallinity (Figure S17), and a decrease in their $N_2$ uptake was observed; the incorporated mass of the PEG chains led to BET surface areas of 865 $m^2\ g^{-1}$ for UiO-66-L1-PEG550 and 521 $m^2\ g^{-1}$ for UiO-66-L1-PEG2000 (Figure 3C). The pore-size distribution of UiO-66-L1-PEG550 corresponds with that reported for UiO-66, but in the case of UiO-66-L1-PEG2000, the adsorption and desorption isotherms reveal a type IV isotherm, typical of mesoporous materials, but with no closure point. In the case of nitrogen

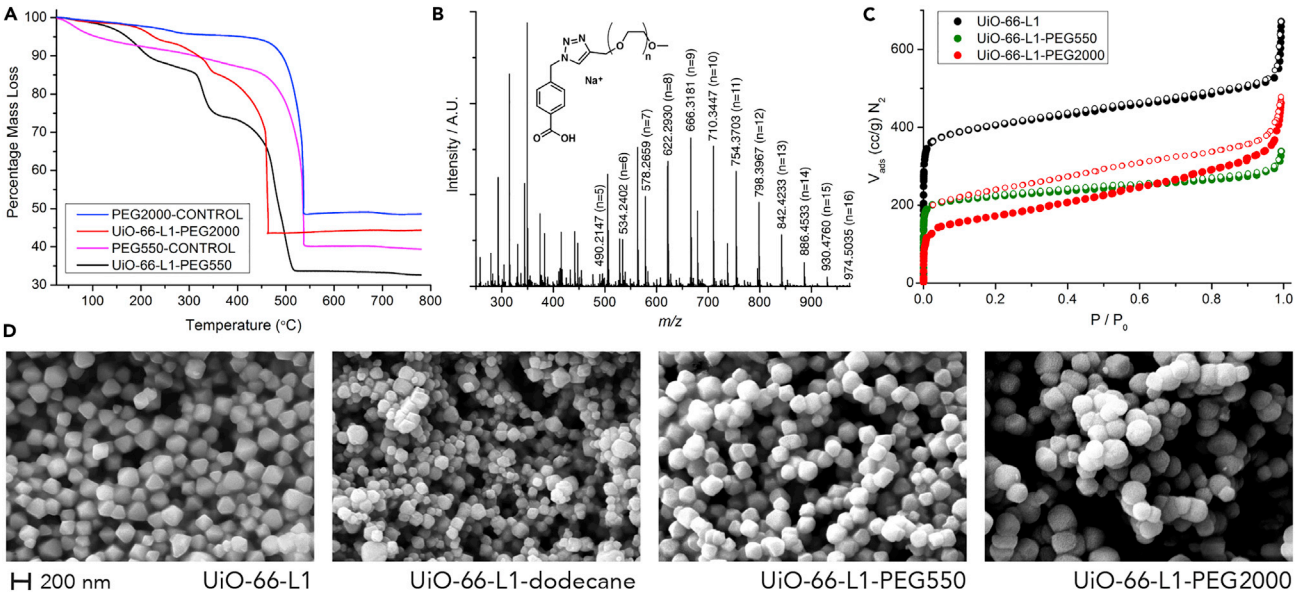


**Figure 3. Surface Modification of UiO-66 with Poly(ethylene glycol)**

(A) TGA profiles of UiO-66-L1-PEG550 and UiO-66-L1-PEG2000 are compared with those of control samples of UiO-66-L1 that had been exposed to propargyl-functionalized PEGs without any Cu(I) catalyst.

(B) HR-ESI-MS of digested UiO-66-L1-PEG550 confirms that the CuAAC reaction took place between the MOF and the PEG chain.

(C) $N_2$ uptake isotherms (77 K) of the PEGylated MOFs. Closed symbols represent adsorption, and empty symbols represent desorption.

(D) SEM images of UiO-66-L1 particles with differing surface functionality show the morphological changes as larger surface units are incorporated by click modulation. The scale bar (200 nm) applies to all images.

adsorption at 77 K, the lower closure point is usually located around $p/p_0 \sim 0.42$, and any hysteresis recorded below this point has been attributed to irreversible changes such as swelling of the adsorbent or surface impurities.[74] A similar phenomenon was found by Wang et al.[43] on UiO-66 functionalization with the phospholipid dihydroxyphenylalanine (DOPA), although to a lesser degree. The fact that PEG2000 chains are considerably bigger in size than DOPA could explain why it is more pronounced in this case.

Interestingly, the physical effects on nanoparticle morphology can be observed by SEM imaging (Figure 3D). As the chain length of the surface functionality increases, the particles become more rounded in shape with less-defined edges and vertices, because their surface features become dominated by the bulk of their capping polymers rather than the underlying MOF crystal structure. Image analysis (Figures S18–S20) also showed a gradual increase in particle size from 146.6 ± 29.3 nm for UiO-66-L1 to 160.2 ± 26.9 nm for UiO-66-L1-PEG550 and 172.9 ± 36.8 nm for UiO-66-L1-PEG2000, consistent with the addition of surface polymer chains of increasing size.

Solution stability and aggregation were investigated by dynamic light scattering (DLS). Measurements in methanol (0.25 mg/mL; Figure S21) showed stable dispersions of PEGylated particles at sizes around 150 nm, correlating well with the SEM data[70] and confirming that no aggregation takes place; in contrast, the unfunctionalized materials UiO-66-AcOH (~800 nm) and UiO-66-L1 (~300 nm) showed aggregation. The power of the surface functionalization protocol was further demonstrated by DLS measurements in aqueous media (Figures S22 and S23). UiO-66-L1 was observed to sediment and precipitate from 0.25 mg/mL aqueous

dispersions over time, with aggregates around 2,000–3,000 nm. UiO-66-L1-PEG550 aggregated to a lesser extent, with stable assemblies around 1,000–1,500 nm, but the larger PEG chains of UiO-66-L1-PEG2000 conferred further dispersive stability, such that assemblies around 250 nm were observed to aggregate to around 400 nm during the experiments. The dependence of aggregation on PEG chain size clearly demonstrates the stabilizing effects of surface modification and the advantages of MOF PEGylation for drug delivery.

In addition, the cytotoxicities of UiO-66-L1-PEG550 and UiO-66-L1-PEG2000, as well as modulators L1 and L2, were assessed by the bioreduction of a tetrazolium compound (MTS), known as the MTS assay (Figures S24 and S25). None of the materials showed any toxicity toward HeLa cells at concentrations up to 1 mg/mL.

The successful covalent surface modification of UiO-66 with both alkyl and PEG chains confirms the versatility and general applicability of the click modulation process. PEG chains have previously been incorporated onto silica-coated UiO-66(Hf), and although this approach facilitated in vivo imaging by computed tomography,[75] it might not be suitable for drug delivery because the silica coating can block access to the pores of the MOF and could affect clearance.

### Degradation Kinetics of PEGylated and Uncoated UiO-66-L1

To be an efficient injectable treatment, the nanocarrier should be stable at the first stages of the treatment; ideally, it should not be degraded in extracellular conditions (i.e., blood [pH 7.4]) in order to avoid renal clearance of the drug yet not be persistent enough to be accumulated over longer treatment periods. The nature of the metal-linker coordination bonds in MOFs ensures total degradation of the structure at sufficiently acidic pH ranges as a result of linker protonation,[76] but strongly coordinating molecules, such as phosphates, are also able to displace the linkers in the structure at extracellular pH.[24] Although the rapid degradation of MOFs under physiological conditions ensures no accumulation of the carrier after it has reached its target and released the drug,[10,77] their instability toward phosphates, which are present in the blood, typically hinders NMOF bioapplications because of fast-release kinetics,[77] and several approaches, such as amorphisation[60] or silica coating,[29,39,75,78] among others, have been studied for improving their stability to phosphate.

The stabilities of UiO-66-L1, UiO-66-L1-PEG550, and UiO-66-L1-PEG2000 were determined in phosphate buffered saline (PBS) at pH 7.4 (Supplemental Information, Section S5) via measurement of the release of bdc linkers by UV-Vis spectroscopy (Figure 4A). L1 was found to have a UV-Vis absorbance profile and extinction coefficient similar to those of bdc and so does not significantly affect the measurements. UiO-66-L1 exhibited an exponential degradation profile reaching a plateau around 85% bdc release after 6 hr of exposure. On the other hand, PEGylated samples exhibited sigmoidal degradation profiles. We observed that the PEG-modified NMOFs degraded at much slower rates during the first 2 hr, after which they reached plateaus similar to those of the uncoated samples at the end of the experiment (Figures S26–S30).

PXRD analysis (Figure 4B) also showed that crystallinity is retained for longer when the samples have been PEGylated, particularly in the first few hours. We expect that the surface corona of covalently attached PEG chains hinders phosphate attack of the $Zr_6$ clusters of the UiO-66 samples, given that the phosphate groups must first diffuse through the PEG coating to reach the zirconium positions, displace the

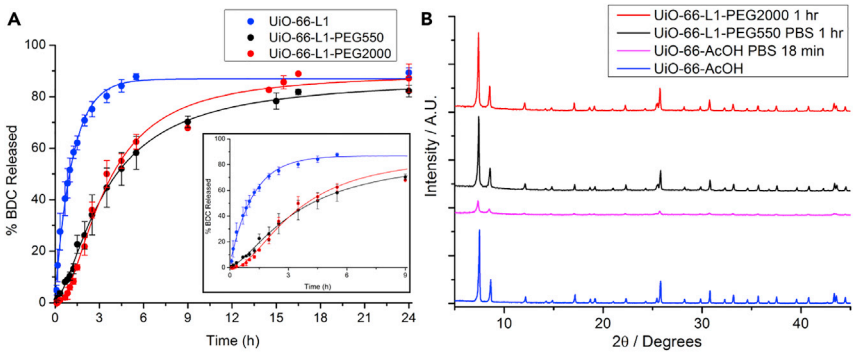


**Figure 4. Enhanced Stability of PEGylated UiO-66**

(A) Degradation profiles of UiO-66-L1, UiO-66-L1-PEG550, and UiO-66-L1-PEG2000 in PBS (pH 7.4). Error bars denote standard deviations from triplicate experiments.

(B) PXRD profiles of the MOFs after immersion in PBS for differing times show the improved stability of the PEGylated MOFs.

modulators and linkers, and coordinate to the zirconium ions similarly to the uncoated NMOF. This enhanced stability means that the burst effect, due to carrier degradation,[79] could be avoided at the first stages of the treatment, improving the treatment efficiency and reducing undesirable side effects while ensuring that the framework can degrade, release cargo, and be cleared over larger periods of exposure.

## Synthesis, Functionalization, and Characterization of Calcein-Containing NMOFs

In order to determine the effect of the PEGylation upon drug-release kinetics and cell internalization routes, we chose calcein as a model drug because of its structural similarities to doxorubicin.[2,60] Calcein is hydrophilic and does not permeate the cell membrane; rather, it requires a drug-delivery vehicle to facilitate its entry into cells. In addition, like doxorubicin, it is a fluorescent molecule, and because of its self-quenching character it can be detected only when it is released from the delivery vector, allowing the measurement of cytoplasmic fluorescence by confocal microscopy or flow cytometry.[80] The versatility of the click modulation technique is further demonstrated by its compatibility with cargo loading (Supplemental Information, Section S6). Simply stirring azide-modified UiO-66-L1 in a concentrated methanolic calcein solution resulted in higher incorporation of calcein (16.0% w/w as determined by UV-Vis spectroscopy) than previously reported in the literature for UiO-66, most likely as a result of the increased porosity of UiO-66-L1.[60] We named the calcein-loaded sample cal@UiO-66-L1. The functionalized modulator L1 remained attached to the MOF framework after calcein uptake, as determined by $^{1}$H NMR spectra of the digested samples, and the azide functionality was used once again to incorporate PEG chains of different lengths according to the CuAAC protocol. Crystallinity was preserved after calcein loading (Figure S32) and PEGylation, and their size, analyzed by SEM, was found not to change (Figure S33). Calcein content was analyzed by UV-Vis spectroscopy and found to be 13.3% w/w for cal@UiO-66-L1-PEG550 and 10.3% w/w for cal@UiO-66-L1-PEG2000 (Figure S34). This confirms that click modulation is compatible with cargo loading, and the decreasing loading values are commensurate with the increasing mass of the particles after PEGylation.

Confirmation of calcein loading by TGA analysis was complicated by the absence of the first calcein thermal decomposition step in the loaded MOF samples

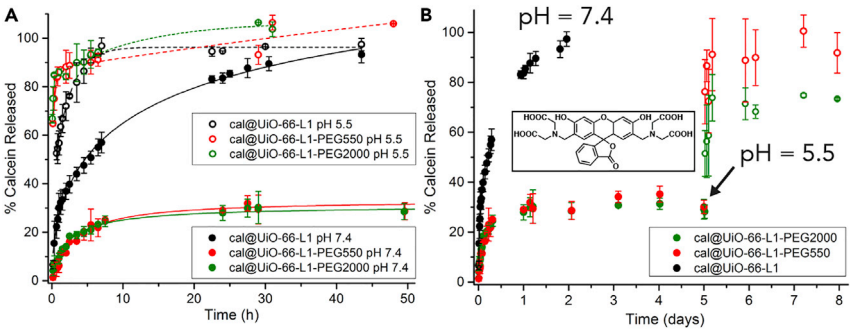


**Figure 5. pH-Responsive Release of Calcein from PEGylated UiO-66**

(A) Calcein-release profiles from UiO-66-L1, UiO-66-L1-PEG550, and UiO-66-L1-PEG2000 in PBS (pH 7.4 and 5.5).

(B) pH-responsive release of calcein from the PEGylated MOFs. Inset: chemical structure of calcein. Error bars denote standard deviations from triplicate experiments.

(Figure S35), indicating that calcein is attached to the external surface and at defect sites. Calcein decomposition occurred over a temperature range similar to that observed previously for PEG groups, making exact quantification troublesome but confirming the presence of the surface PEG functionality in cal@UiO-66-L1-PEG550 and cal@UiO-66-L1-PEG2000 (Figure S36). $N_2$ adsorption isotherms (77 K) confirmed that cal@UiO-66-L1 exhibited a decrease in surface area ($S_{BET}$ = 1,002 $m^2\ g^{-1}$) but maintained the pore-size distribution characteristic of UiO-66, again suggesting that calcein is not significantly blocking the pores but attaching to the particle surface and localizing at defects (Figure S37). The porosity of both PEGylated calcein-loaded samples ($S_{BET}$ = 826 $m^2\ g^{-1}$ for cal@UiO-66-L1-PEG550 and $S_{BET}$ = 683 $m^2\ g^{-1}$ for cal@UiO-66-L1-PEG2000) decreased similarly to that of the empty PEGylated UiO-66-L1 samples, confirming PEG surface attachment can occur without displacing molecular cargo.

## pH-Dependent Calcein-Release Profiles

The effect of surface modification on calcein release was monitored in PBS at pH 7.4 and 5.5 according to a UV-Vis spectrophotometric analysis protocol similar to the degradation experiments (Supplemental Information, Section S7). Monitoring release at different pH values is very important given that extracellular pH is ~7.4, intracellular pH is ~6.8, and the pH of cancer cells is close to 5.5,[81] providing a potential mechanism for targeted drug delivery. The release of calcein from both coated and uncoated samples was affected by the pH (Figure 5A); however, the release at pH 7.4 was drastically decreased for the PEGylated samples. Both cal@UiO-66-L1-PEG550 and cal@UiO-66-L1-PEG2000 initially released calcein slowly at pH 7.4 and did not release more than ~30% of their total cargo after 5 days. In contrast, they rapidly released ~80% of cargo within an hour at pH 5.5 and released nearly the full amount in pH 5.5 after 2 days (Figures S38–S50).

If this behavior can be retained in vivo, PEGylated UiO-66 samples could be expected to store the majority of cargo in extracellular conditions and thus avoid the non-selective distribution of therapeutics while being able to release it once it has reached its target. The stimuli-responsive release of calcein from the PEGylated MOFs was therefore assessed by a similar experiment, where the pH of the PBS solution was adjusted from 7.4 to 5.5 after 5 days (Figure 5B). An immediate, rapid release of calcein was observed, whereby slightly less calcein was released from

UiO-66-L1-PEG2000 than from the analog with the shorter chain. Nonetheless, this result is highly promising for drug-delivery applications should the particles be efficiently internalized by cells.

To gain further insight into the mechanism of release, we subjected samples of the MOFs to simulated release conditions at pH 7.4: cal@UiO-66-L1 after 1 day and cal@UiO-66-L1-PEG2000 after 2 days (Supplemental Information, Section S8). The amount of calcein released from both individual experiments determined by UV-Vis spectroscopy (67.5% from cal@UiO-66-L1 and 42.7% from cal@UiO-66-L1-PEG2000) is in concordance with the release profiles. Both samples showed a decrease in crystallinity by PXRD after calcein release, although the characteristic UiO-66 reflection peaks could be determined (Figure S51), meaning that the core of the materials remained crystalline. TGA showed the disappearance of the PEG moiety from cal@UiO-66-L1-PEG2000 and an increase on the metal residue for both samples (Figure S52), suggesting some degradation. Both samples remained porous (Figure S53); the surface area of cal@UiO-66-L1 ($S_{BET}$ = 1,155 $m^2$ $g^{-1}$) increased from the release of significant amounts of calcein mass, and the surface area of cal@UiO-66-L1-PEG2000 ($S_{BET}$ = 554 $m^2$ $g^{-1}$) decreased slightly, possibly because of pore blocking or the incorporation of additional mass, such as phosphates.

We hypothesize that, at pH 7.4, the phosphates present in PBS attack the zirconium positions[24] and displace the surface ligands and the calcein. When UiO-66 is not PEGylated, the MOF is much more accessible (both internally and externally) and therefore so are the zirconium clusters, enabling a faster exchange between phosphates and ligands, modulators, and calcein. On the other hand, for surface-modified cal@UiO-66-L1-PEG2000, the phosphates must diffuse through the PEG coating before reaching the MOF. We hypothesize that a corona of coordinating phosphates is then formed, obstructing the MOF and hindering further phosphate attack to release remaining calcein molecules. Indeed, FT-IR spectra of cal@UiO-66-L1-PEG2000 after 1 day in PBS at pH 7.4 showed more significant signals for phosphates than for cal@UiO-66-L1 under the same conditions (Figure S54), suggesting that the PEG coating induces a corona build-up and that unmodified UiO-66 simply undergoes surface exchange (Supplemental Information, Section S8). When the pH is more acidic, the carboxylate units of bdc ligands, surface functionality, and calcein are easier to protonate, and therefore MOF degradation and calcein release are much more pronounced.[76]

## Endocytosis Studies

Confocal fluorescence microscopy has been used to confirm successful internalization of the MOF nanoparticles by HeLa cells and subsequent calcein release (Supplemental Information, Section S9). Figure 6 shows the confocal microscopy images of HeLa cells incubated with, from top to bottom, nothing (control), free calcein, cal@UiO-66-L1, cal@UiO-66-L1-PEG550, and cal@UiO-66-L1-PEG2000. We used Hoechst 33342 (H33342) and CellMask to stain the nucleus and membrane of the cells, respectively. We used CellMask as a viability control to probe the cell membrane integrity and show that the MOFs were inside the cells. The effectiveness of calcein as a probe is demonstrated by the fact that free calcein was not taken up by cells, in concert with previous reports,[60,80,82] so any green fluorescence within cells comes from released calcein from internalized MOF materials. UiO-66-L1, UiO-66-L1-PEG550, and UiO-66-L1-PEG2000 all transported calcein into HeLa cells, as seen by the green fluorescence, whereas the control cells and those incubated with free calcein showed no signal.

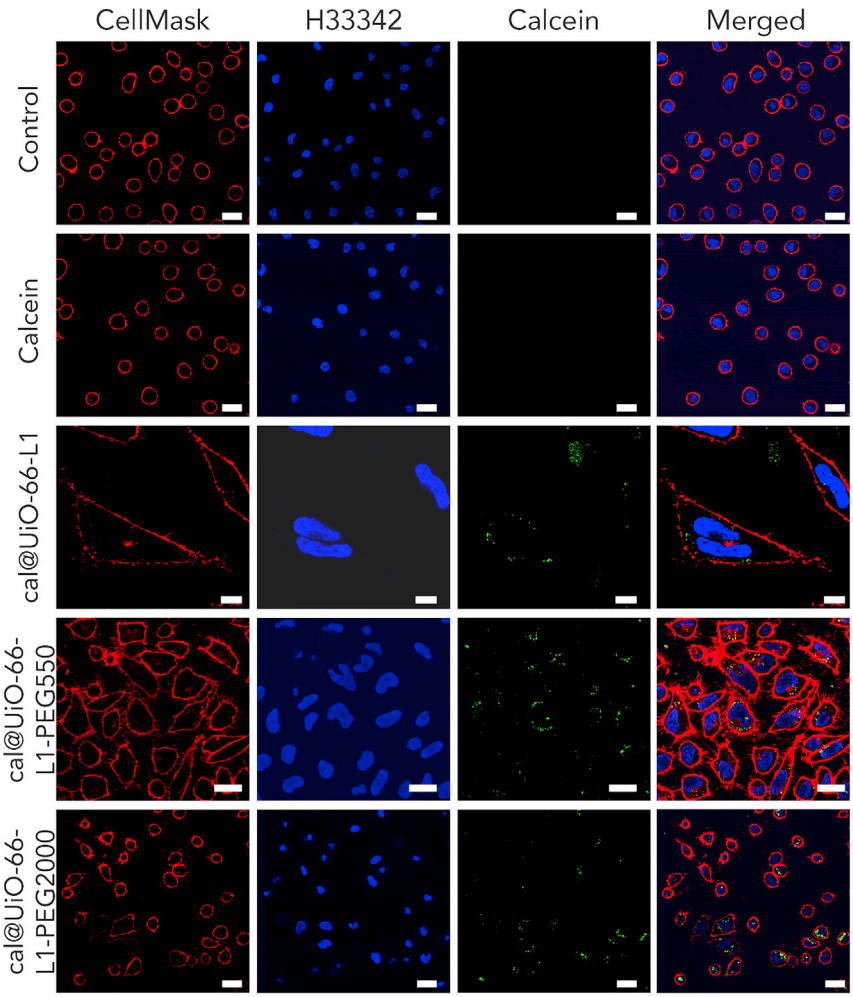


**Figure 6. Confocal Microscopy Images of HeLa Cells Incubated with Different Materials**

From top to bottom: control, free calcein, cal@UiO-66-L1, cal@UiO-66-L1-PEG550, and cal@UiO-66-L1-PEG2000. Cells were subsequently stained with Hoechst 33342 (5 μg/mL) and CellMask orange (1×). Scale bars represent 25 μm in all images except for cal@UiO-66-L1, in which it represents 10 μm.

The transport of calcein into NMOFs allows the study of endocytosis pathways by fluorescence-activated cell sorting (FACS). There are three main classes of endocytosis pathways: (1) clathrin-mediated, (2) caveolae-mediated, and (3) clathrin- and caveolae-independent endocytosis such as macropinocytosis.[38,83,84] Clathrin-mediated endocytosis involves recognition of the cargo by cell-surface receptors, which internalize it into protein (clathrin)-coated vesicles 60–200 nm in size, called early endosomes.[85] These early endosomes then mature into late endosomes and finally fuse with lysosomes, causing degradation of the drug-delivery system along with its loaded cargo, thus nullifying its therapeutic effect.[85] On the other hand, caveolae-mediated endocytosis is associated with the formation of lipid-raft-enriched flask-shaped invaginations (50–100 nm) coated with a protein called caveolin.[86] Particles internalized via caveolae-mediated endocytosis can later be delivered to different locations in a cell, including a pH-neutral compartment called the caveosome, and then transported to a final intracellular location, potentially avoiding lysosomal degradation.[87,88]

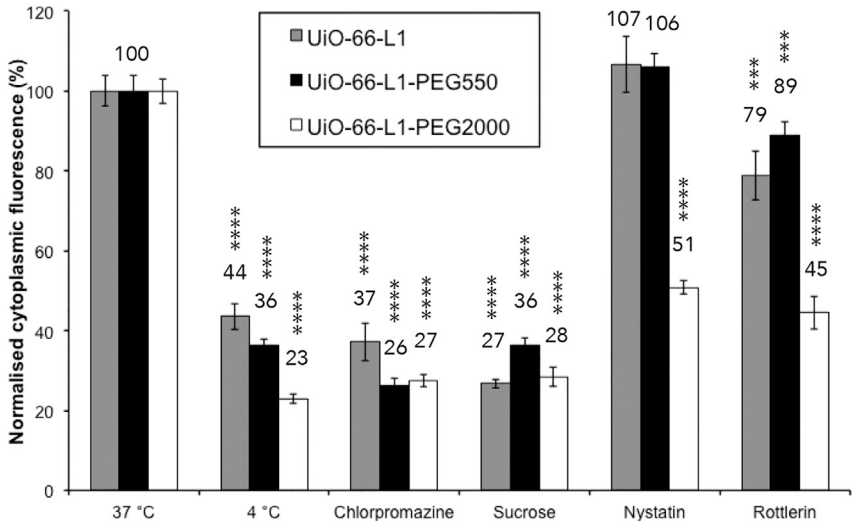


**Figure 7. Effects of Pharmacological Endocytosis Inhibitors on the Uptake of cal@UiO-66-L1, cal@UiO-66-L1-PEG550, and cal@UiO-66-L1-PEG2000 into HeLa Cells, as Measured by FACS**

The statistical significance was determined by ordinary one-way ANOVA and is indicated on the graph: ***$p < 0.001$ and ****$p < 0.0001$.

To study the internalization routes of the PEGylated and unPEGylated NMOFs, we used different pharmacologic inhibitors according to our previous work (Supplemental Information, Section S9).[38] First, we used sucrose[89] and chlorpromazine[90] to independently inhibit the clathrin-mediated pathway. Second, we used nystatin to inhibit the caveolae-mediated pathway.[91] Finally, we employed rottlerin[92,93] to prevent macropinocytosis. Tracers known to selectively follow each pathway were used as positive controls for the inhibitors: transferrin and ceramide for clathrin- and caveolae-mediated pathways, respectively, and dextran for macropinocytosis. Cells were incubated with each inhibitor for 30 min and then for 90 min together with the NMOF (Supplemental Information, Section S9). Because nanoparticle size is known to affect cell internalization routes,[38] for example, the recent report of enhanced uptake of 90 nm nanoparticles of a Zr-porphyrin MOF into HeLa cells,[94] we performed all experiments on one base batch of UiO-66-L1, surface modified and loaded as necessary, to ensure that particle size was relatively homogeneous.

Figure 7 shows the normalized internal fluorescence, obtained through FACS, of HeLa cells after the uptake of cal@UiO-66-L1, cal@UiO-66-L1-PEG550, and cal@UiO-66-L1-PEG2000 in the presence and absence of the pharmacologic endocytosis inhibitors. The uptake of all three particles at 4°C was significantly reduced, which confirms that they are internalized via an energy-dependent endocytosis process. The uptake of cal@UiO-66-L1 after exposure to sucrose and chlorpromazine was reduced to ~27% ± 1% and 37% ± 5%, respectively, whereas exposure to nystatin had no effect (~107% ± 7%), revealing that the unfunctionalized MOF is not internalized through the caveolae-mediated route. Rottlerin decreased its uptake to ~79% ± 6%. For cal@UiO-66-L1-PEG550, the uptake after exposure to sucrose and chlorpromazine decreased to ~36% ± 2% and 26% ± 2%, respectively, whereas there was no reduction in uptake upon exposure to nystatin (~106% ± 3%). Rottlerin slightly decreased the uptake to ~89% ± 4%. These values are similar to those for cal@UiO-66-L1, suggesting that the PEG550 coating did not affect the route of endocytosis.

Finally, for cal@UiO-66-L1-PEG2000, exposing the cells to sucrose and chlorpromazine decreased the uptake to ~28% ± 2% and 27% ± 2%, respectively. Interestingly, significant changes were found, whereby nystatin and rottlerin reduced the uptake to ~51% ± 2% and 45% ± 4%, respectively, showing that the PEGylated MOF is partially internalized through caveolae-mediated endocytosis. This indicates that the UiO-66 internalization pathway is significantly affected by the functionality attached to its surface, and the longer PEG chains ($M_n$ ~ 2,000) allow the NMOFs to partially avoid lysosomal degradation. The amphiphilic nature of cal@UiO-66-L1-PEG2000, in contrast to the hydrophilic surface of the uncoated sample, is thought to be more compatible with the caveolae-mediated route. In addition, part of the cellular trafficking of all three MOFs occurs through macropinocytosis because the uptake is affected by the presence of rottlerin. However, this is a non-selective process allowing the internalization of large quantities of material independently of its constitution.[95] Macropinocytosis could be a consequence of aggregation of nanoparticles if the effects observed by DLS also occur in this more dilute environment, although it has not been observed as a significant pathway for the other NMOF samples, which exhibit greater aggregation than UiO-66-L1-PEG2000.

We used laser confocal microscopy with LysoTracker-Deep red to qualitatively determine the degree of co-localization between the calcein-loaded NMOF particles (green) and the lysosomes (Figure S56). After 2 hr of incubation, a high level of co-localization was found for all three MOFs, given that FACS confirmed that clathrin-mediated uptake took place in all NMOFs. However, in the case of cal@UiO-66-L1-PEG2000, a higher degree of localized light-green particles outside the lysosomes was also observed, suggesting altered uptake mechanisms.

### Therapeutic Efficacy of Drug-Loaded NMOFs

To investigate the effect of this alternative uptake mechanism and particle stability on the therapeutic efficacy of the PEGylated NMOFs, we selected dichloroacetic acid (DCA) for delivery because it is an anticancer drug that is cytotoxic only once it is internalized by cells.[96] DCA turns on the apoptosis systems of cancer cells, which is otherwise suppressed, thus allowing them to die.[97,98] However, its hydrophilicity means it is rapidly cleared with a half-life from the first dose of less than 1 hr, and it can induce neurotoxicity by crossing the blood-brain barrier,[99] so DCA is well suited for use in a nanocarrier system.

DCA was added (Supplemental Information, Section S10) to hydrothermal syntheses in place of acetic acid to yield DCA@UiO-66-L1. The presence of both DCA and L1 was confirmed by $^1$H NMR spectroscopy (Figure S57), and the 150 nm particles observed by SEM were found to be crystalline by PXRD (Figure S58). The material was PEGylated under the CuAAC conditions used previously to yield DCA@UiO-66-L1-PEG2000. TGA confirmed the presence of the PEG chain and allowed an estimation of DCA loading; these values were confirmed by inductively coupled plasma mass spectrometry for measuring the chlorine content, giving DCA loadings of 13.7% w/w for DCA@UiO-66-L1 and 12.1% w/w for DCA@UiO-66-L1-PEG2000 (Figure S59). The cytotoxicities of the two materials were determined by MTS assay (Figure 8) against HeLa cells, where it was found that the PEGylated material induced significant cell death at NMOF concentrations of 0.75 mg/mL and above, whereas the uncoated material did not. In comparison, DCA alone has been found to have an $IC_{50}$ of 23.0 ± 4.0 mM against methylcholanthrene fibrosarcoma cells, a considerably higher dose.[98] We expect that the enhanced stability and cellular internalization of the PEGylated MOF contributes significantly to the improved therapeutic effect.

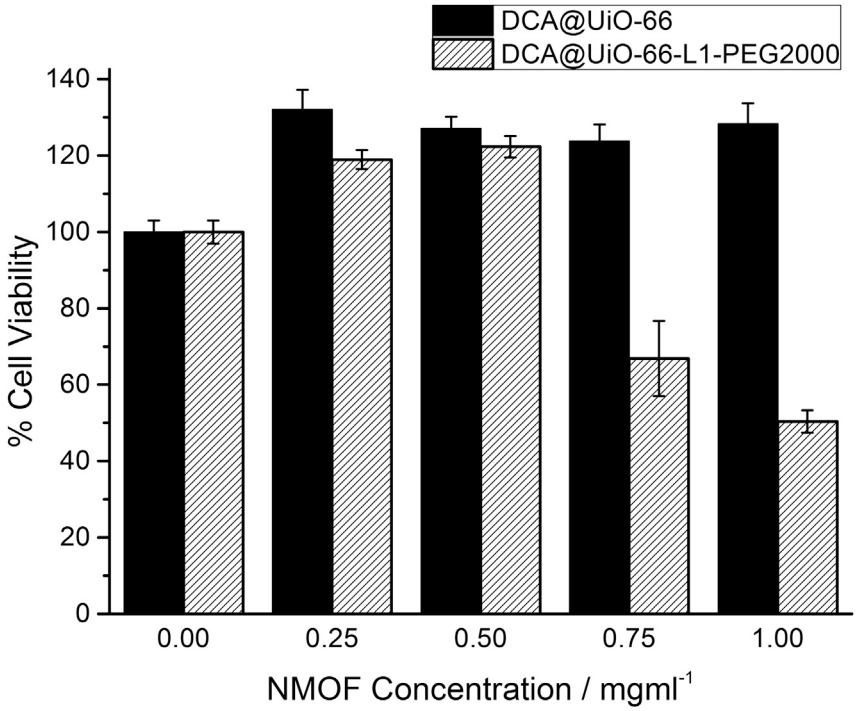


**Figure 8. Metabolic Activity of HeLa Cells after 72 hr of Exposure to DCA@UiO-66-L1 and DCA@UiO-66-L1-PEG2000, as Measured by MTS Assay**

## Conclusions

We have presented a reproducible and innovative protocol—click modulation—to selectively introduce surface functionality to the Zr MOF UiO-66. A range of experiments have shown that differing chemical functionality can be incorporated in the MOF via the CuAAC reaction with functionalized modulators and that the two-stage process is compatible with cargo loading. Surface modification has been shown to be of prime importance for drug-delivery applications, specifically for UiO-66 nanoparticles loaded with calcein or DCA and coated with PEG chains of different lengths.

PEGylation has been shown to improve the stability of UiO-66 toward phosphate-induced degradation and dispersion in aqueous media, and calcein release has been proven to be pH dependent. In contrast to bare nanoparticles, PEGylated UiO-66 samples did not release more than ~40% of their calcein cargo after 5 days at pH 7.4, yet they released the full amount after 2 days in pH 5.5. In addition, pH-responsive release was achieved in this pH region, mirroring the change in conditions from blood-stream circulation to cancer cellular internalization to allow stimuli-responsive drug delivery. The surface chemistry also altered the cell-uptake routes of the nanoparticles; coating UiO-66 with PEG2000 enhanced caveolae-mediated endocytosis, allowing the NMOF to partially escape the lysosome, thus avoiding degradation of the drug and improving the possibility of reaching other cellular organelles. This effect was dependent on the length of the PEG chain; UiO-66 modified with PEG550 did not exhibit similarly enhanced caveolae-mediated uptake. PEGylation is compatible with loading of the anticancer drug DCA, and compared with DCA@UiO-66-L1, DCA@UiO-66-L1-PEG2000 exhibits significant cytotoxicity at concentrations above 0.75 mg/mL, possibly as a consequence of the differing cell-uptake routes, and enhances the therapeutic effect of DCA.

It is clear that functionalizing MOF nanoparticles with polymer chains can dramatically improve their suitability for biological applications. Our own results show improved stability, drug release, and cell-uptake properties with biocompatible PEG chains, and recent work has shown that polyaniline-modified UiO-66 is effective and safe for anticancer photothermal therapy.[100] We expect the versatility of the click modulation protocol to allow a variety of MOFs to be selectively surface functionalized with a variety of chemical units and have immediate application not only in biomedical settings but also in selective adsorption and separation processes and catalysis. Indeed, during the course of our study, a similar technique was applied to the functionalization of covalent organic frameworks.[101]

## EXPERIMENTAL PROCEDURES

Full experimental procedures are provided in the Supplemental Information.

## SUPPLEMENTAL INFORMATION

Supplemental Information includes Supplemental Experimental Procedures, 60 figures, and 2 tables and can be found with this article online at http://dx.doi.org/10.1016/j.chempr.2017.02.005.

## AUTHOR CONTRIBUTIONS

Conceptualization, R.S.F.; Methodology, R.S.F. and D.F.-J.; Investigation, I.A.L., S.H., S.S., and C.O.-T.; Writing – Original Draft, I.A.L. and R.S.F.; Writing – Review & Editing, I.A.L., S.H., S.S., C.O.-T., D.F.-J., and R.S.F.; Supervision, R.S.F. and D.F.-J.; Project Administration, R.S.F. and D.F.-J.; Funding Acquisition, R.S.F.

## ACKNOWLEDGMENTS

R.S.F. and D.F.-J. thank the Royal Society for the receipt of University Research Fellowships. R.S.F. and I.A.L. thank the University of Glasgow for funding. This project received funding in part from the European Research Council (ERC) under the European Union's Horizon 2020 Programme for Research and Innovation (grant agreement no. 677289, SCoTMOF, ERC-2015-STG).

Received: September 30, 2016
Revised: November 15, 2016
Accepted: February 14, 2017
Published: April 13, 2017

## REFERENCES AND NOTES

1. Castaing, N., Merlet, D., and Cambar, J. (1990). Cis-platin cytotoxicity in human and rat tubular cell cultures. Toxicol. In Vitro *4*, 396–398.

2. Poljaková, J., Eckschlager, T., Hřebačková, J., Hraběta, J., and Stiborová, M. (2008). The comparison of cytotoxicity of the anticancer drugs doxorubicin and ellipticine to human neuroblastoma cells. Interdiscip. Toxicol. *1*, 186.

3. Sun, C.C., Bodurka, D.C., Weaver, C.B., Rasu, R., Wolf, J.K., Bevers, M.W., Smith, J.A., Wharton, J.T., and Rubenstein, E.B. (2005). Rankings and symptom assessments of side effects from chemotherapy: insights from experienced patients with ovarian cancer. Support. Care Cancer *13*, 219.

4. Rocca, J.D., Liu, D., and Lin, W. (2011). Nanoscale metal–organic frameworks for biomedical imaging and drug delivery. Acc. Chem. Res. *44*, 957.

5. Krukiewicz, K., and Zak, J.K. (2016). Biomaterial-based regional chemotherapy: local anticancer drug delivery to enhance chemotherapy and minimize its side-effects. Mater. Sci. Eng. C Mater. Biol. Appl. *62*, 927.

6. Peer, D., Karp, J.M., Hong, S., Farokhzad, O.C., Margalit, R., and Langer, R. (2007). Nanocarriers as an emerging platform for cancer therapy. Nat. Nano *2*, 751.

7. Dobrovolskaia, M.A., and McNeil, S.E. (2007). Immunological properties of engineered nanomaterials. Nat. Nano *2*, 469.

8. Qu, G., Zhang, C., Yuan, L., He, J., Wang, Z., Wang, L., Liu, S., and Jiang, G. (2012). Quantum dots impair macrophagic morphology and the ability of phagocytosis by inhibiting the Rho-associated kinase signaling. Nanoscale *4*, 2239.

9. Horcajada, P., Chalati, T., Serre, C., Gillet, B., Sebrie, C., Baati, T., Eubank, J.F., Heurtaux, D., Clayette, P., Kreuz, C., et al. (2010). Porous metal-organic-framework nanoscale carriers as a potential platform for drug delivery and imaging. Nat. Mater. *9*, 172.

10. McKinlay, A.C., Morris, R.E., Horcajada, P., Férey, G., Gref, R., Couvreur, P., and Serre, C. (2010). BioMOFs: metal–organic frameworks for biological and medical applications. Angew. Chem. Int. Ed. *49*, 6260.

11. Maruyama, K. (2011). Intracellular targeting delivery of liposomal drugs to solid tumors based on EPR effects. Adv. Drug Deliv. Rev. *63*, 161.

12. Sur, S., Fries, A.C., Kinzler, K.W., Zhou, S., and Vogelstein, B. (2014). Remote loading of preencapsulated drugs into stealth liposomes. Proc. Natl. Acad. Sci. USA *111*, 2283.

13. Morabito, J.V., Chou, L.-Y., Li, Z., Manna, C.M., Petroff, C.A., Kyada, R.J., Palomba, J.M., Byers, J.A., and Tsung, C.-K. (2014). Molecular encapsulation beyond the aperture size limit through dissociative linker exchange in metal–organic framework crystals. J. Am. Chem. Soc. *136*, 12540.

14. Canton, I., and Battaglia, G. (2012). Endocytosis at the nanoscale. Chem. Soc. Rev. *41*, 2718.

15. Chithrani, B.D., Ghazani, A.A., and Chan, W.C.W. (2006). Determining the size and shape dependence of gold nanoparticle uptake into mammalian cells. Nano. Lett. *6*, 662.

16. Yuan, F., Dellian, M., Fukumura, D., Leunig, M., Berk, D.A., Torchilin, V.P., and Jain, R.K. (1995). Vascular permeability in a human tumor xenograft: molecular size dependence and cutoff size. Cancer Res. *55*, 3752.

17. Wu, P.-C., Shieh, D.-B., and Cheng, F.-Y. (2014). Nanomaterial-mediated photothermal cancer treatment: the pivotal role of cellular uptake on photothermal therapeutic efficacy. RSC Adv. *4*, 53297.

18. Yin Win, K., and Feng, S.-S. (2005). Effects of particle size and surface coating on cellular uptake of polymeric nanoparticles for oral delivery of anticancer drugs. Biomaterials *26*, 2713.

19. Arora, S., Rajwade, J.M., and Paknikar, K.M. (2012). Nanotoxicology and in vitro studies: the need of the hour. Toxicol. Appl. Pharmacol. *258*, 151.

20. Tamames-Tabar, C., Cunha, D., Imbuluzqueta, E., Ragon, F., Serre, C., Blanco-Prieto, M.J., and Horcajada, P. (2014). Cytotoxicity of nanoscaled metal-organic frameworks. J. Mater. Chem. B *2*, 262.

21. Lee, J., Farha, O.K., Roberts, J., Scheidt, K.A., Nguyen, S.T., and Hupp, J.T. (2009). Metal-organic framework materials as catalysts. Chem. Soc. Rev. *38*, 1450.

22. Cousin Saint Remi, J., Rémy, T., Van Hunskerken, V., van de Perre, S., Duerinck, T., Maes, M., De Vos, D., Gobechiya, E., Kirschhock, C.E.A., Baron, G.V., and Denayer, J.F.M. (2011). Biobutanol separation with the metal–organic framework ZIF-8. ChemSusChem *4*, 1074.

23. Horcajada, P., Gref, R., Baati, T., Allan, P.K., Maurin, G., Couvreur, P., Férey, G., Morris, R.E., and Serre, C. (2012). Metal–organic frameworks in biomedicine. Chem. Rev. *112*, 1232.

24. Bellido, E., Hidalgo, T., Lozano, M.V., Guillevic, M., Simón-Vázquez, R., Santander-Ortega, M.J., González-Fernández, Á., Serre, C., Alonso, M.J., and Horcajada, P. (2015). Heparin-engineered mesoporous iron metal-organic framework nanoparticles: toward stealth drug nanocarriers. Adv. Healthc. Mater. *4*, 1246.

25. Horcajada, P., Chevreau, H., Heurtaux, D., Benyettou, F., Salles, F., Devic, T., Garcia-Marquez, A., Yu, C., Lavrard, H., Dutson, C.L., et al. (2014). Extended and functionalized porous iron(iii) tri- or dicarboxylates with MIL-100/101 topologies. Chem. Commun. *50*, 6872.

26. Huxford, R.C., Rocca, J.D., and Lin, W. (2010). Metal-organic frameworks as potential drug carriers. Curr. Opin. Chem. Biol. *14*, 262.

27. Cunha, D., Ben Yahia, M., Hall, S., Miller, S.R., Chevreau, H., Elkaïm, E., Maurin, G., Horcajada, P., and Serre, C. (2013). Rationale of drug encapsulation and release from biocompatible porous metal–organic frameworks. Chem. Mater. *25*, 2767.

28. Liu, D., Huxford, R.C., and Lin, W. (2011). Phosphorescent nanoscale coordination polymers as contrast agents for optical imaging. Angew. Chem. Int. Ed. *50*, 3696.

29. Rowe, M.D., Thamm, D.H., Kraft, S.L., and Boyes, S.G. (2009). Polymer-modified gadolinium metal-organic framework nanoparticles used as multifunctional nanomedicines for the targeted imaging and treatment of cancer. Biomacromolecules *10*, 983.

30. Zhu, X., Gu, J., Wang, Y., Li, B., Li, Y., Zhao, W., and Shi, J. (2014). Inherent anchorages in UiO-66 nanoparticles for efficient capture of alendronate and its mediated release. Chem. Commun. *50*, 8779.

31. Wang, W., Wang, L., Li, Z., and Xie, Z. (2016). BODIPY-containing nanoscale metal-organic frameworks for photodynamic therapy. Chem. Commun. *52*, 5402.

32. Zhao, H.-X., Zou, Q., Sun, S.-K., Yu, C., Zhang, X., Li, R.-J., and Fu, Y.-Y. (2016). Theranostic metal-organic framework core-shell composites for magnetic resonance imaging and drug delivery. Chem. Sci. *7*, 5294.

33. Miller, S.E., Teplensky, M.H., Moghadam, P.Z., and Fairen-Jimenez, D. (2016). Metal-organic frameworks as biosensors for luminescence-based detection and imaging. Interface Focus *6*, 20160027.

34. Yaghi, O.M., O'Keeffe, M., Ockwig, N.W., Chae, H.K., Eddaoudi, M., and Kim, J. (2003). Reticular synthesis and the design of new materials. Nature *423*, 705.

35. Kitagawa, S., Kitaura, R., and Noro, S.-I. (2004). Functional porous coordination polymers. Angew. Chem. Int. Ed. *43*, 2334.

36. Iversen, T.-G., Skotland, T., and Sandvig, K. (2011). Endocytosis and intracellular transport of nanoparticles: present knowledge and need for future studies. Nano Today *6*, 176.

37. Oh, N., and Park, J.H. (2014). Endocytosis and exocytosis of nanoparticles in mammalian cells. Int. J. Nanomedicine *9*, 51.

38. Orellana-Tavra, C., Mercado, S.A., and Fairen-Jimenez, D. (2016). Endocytosis mechanism of nano metal-organic frameworks for drug delivery. Adv. Healthc. Mater. *5*, 2261.

39. Wang, Z., and Cohen, S.M. (2009). Postsynthetic modification of metal-organic frameworks. Chem. Soc. Rev. *38*, 1315.

40. Kim, M., Cahill, J.F., Fei, H., Prather, K.A., and Cohen, S.M. (2012). Postsynthetic ligand and cation exchange in robust metal–organic frameworks. J. Am. Chem. Soc. *134*, 18082.

41. Marshall, R.J., Richards, T., Hobday, C.L., Murphie, C.F., Wilson, C., Moggach, S.A., Bennett, T.D., and Forgan, R.S. (2016). Postsynthetic bromination of UiO-66 analogues: altering linker flexibility and mechanical compliance. Dalton Trans. *45*, 4132.

42. Ragon, F., Campo, B., Yang, Q., Martineau, C., Wiersum, A.D., Lago, A., Guillerm, V., Hemsley, C., Eubank, J.F., Vishnuvarthan, M., et al. (2015). Acid-functionalized UiO-66(Zr) MOFs and their evolution after intra-framework cross-linking: structural features and sorption properties. J. Mater. Chem. A. *3*, 3294.

43. Wang, S., Morris, W., Liu, Y., McGuirk, C.M., Zhou, Y., Hupp, J.T., Farha, O.K., and Mirkin, C.A. (2015). Surface-specific functionalization of nanoscale metal–organic frameworks. Angew. Chem. Int. Ed. *54*, 14738.

44. Gross, A.F., Sherman, E., Mahoney, S.L., and Vajo, J.J. (2013). Reversible ligand exchange in a metal–organic framework (MOF): toward MOF-based dynamic combinatorial chemical systems. J. Phys. Chem. A. *117*, 3771.

45. Kondo, M., Furukawa, S., Hirai, K., and Kitagawa, S. (2010). Coordinatively immobilized monolayers on porous coordination polymer crystals. Angew. Chem. Int. Ed. *49*, 5327.

46. McGuire, C.V., and Forgan, R.S. (2015). The surface chemistry of metal-organic frameworks. Chem. Commun. *51*, 5199.

47. Zacher, D., Schmid, R., Wöll, C., and Fischer, R.A. (2011). Surface chemistry of metal–organic frameworks at the liquid–solid interface. Angew. Chem. Int. Ed. *50*, 176.

48. Wuttke, S., Braig, S., Prei, Zimpel, A., Sicklinger, J., Bellomo, C., Radler, J.O., Vollmar, A.M., and Bein, T. (2015). MOF nanoparticles coated by lipid bilayers and their uptake by cancer cells. Chem. Commun. *51*, 15752.

49. Férey, G., Serre, C., Mellot-Draznieks, C., Millange, F., Surblé, S., Dutour, J., and Margiolaki, I. (2004). A hybrid solid with giant pores prepared by a combination of targeted chemistry, simulation, and powder diffraction. Angew. Chem. Int. Ed. *43*, 6296.

50. Taylor-Pashow, K.M.L., Rocca, J.D., Xie, Z., Tran, S., and Lin, W. (2009). Post-synthetic modifications of iron-carboxylate nanoscale metal-organic frameworks for imaging and drug delivery. J. Am. Chem. Soc. *131*, 14261.

51. Guo, H., Zhu, Y., Wang, S., Su, S., Zhou, L., and Zhang, H. (2012). Combining coordination modulation with acid–base adjustment for the control over size of metal–organic frameworks. Chem. Mater. *24*, 444.

52. Tsuruoka, T., Furukawa, S., Takashima, Y., Yoshida, K., Isoda, S., and Kitagawa, S. (2009). Nanoporous nanorods fabricated by

coordination modulation and oriented attachment growth. Angew. Chem. Int. Ed. *48*, 4739.

53. Vermoortele, F., Bueken, B., Le Bars, G., Van de Voorde, B., Vandichel, M., Houthoofd, K., Vimont, A., Daturi, M., Waroquier, M., Van Speybroeck, V., et al. (2013). Synthesis modulation as a tool to increase the catalytic activity of metal–organic frameworks: the unique case of UiO-66(Zr). J. Am. Chem. Soc. *135*, 11465.

54. Umemura, A., Diring, S., Furukawa, S., Uehara, H., Tsuruoka, T., and Kitagawa, S. (2011). Morphology design of porous coordination polymer crystals by coordination modulation. J. Am. Chem. Soc. *133*, 15506.

55. Pham, M.-H., Vuong, G.-T., Vu, A.-T., and Do, T.-O. (2011). Novel route to size-controlled Fe–MIL-88B–$NH_2$ metal–organic framework nanocrystals. Langmuir *27*, 15261.

56. Hermes, S., Witte, T., Hikov, T., Zacher, D., Bahnmüller, S., Langstein, G., Huber, K., and Fischer, R.A. (2007). Trapping metal-organic framework nanocrystals: an in-situ time-resolved light scattering study on the crystal growth of MOF-5 in solution. J. Am. Chem. Soc. *129*, 5324.

57. Park, J., Wang, Z.U., Sun, L.-B., Chen, Y.-P., and Zhou, H.-C. (2012). Introduction of functionalized mesopores to metal–organic frameworks via metal–ligand–fragment coassembly. J. Am. Chem. Soc. *134*, 20110.

58. Zimpel, A., Preiß, T., Röder, R., Engelke, H., Ingrisch, M., Peller, M., Rädler, J.O., Wagner, E., Bein, T., Lächelt, U., and Wuttke, S. (2016). Imparting functionality to MOF nanoparticles by external surface selective covalent attachment of polymers. Chem. Mater. *28*, 3318.

59. Cavka, J.H., Jakobsen, S., Olsbye, U., Guillou, N., Lamberti, C., Bordiga, S., and Lillerud, K.P. (2008). A new zirconium inorganic building brick forming metal organic frameworks with exceptional stability. J. Am. Chem. Soc. *130*, 13850.

60. Orellana-Tavra, C., Baxter, E.F., Tian, T., Bennett, T.D., Slater, N.K.H., Cheetham, A.K., and Fairen-Jimenez, D. (2015). Amorphous metal-organic frameworks for drug delivery. Chem. Commun. *51*, 13878.

61. Liang, W., and D'Alessandro, D.M. (2013). Microwave-assisted solvothermal synthesis of zirconium oxide based metal-organic frameworks. Chem. Commun. *49*, 3706.

62. Katz, M.J., Brown, Z.J., Colon, Y.J., Siu, P.W., Scheidt, K.A., Snurr, R.Q., Hupp, J.T., and Farha, O.K. (2013). A facile synthesis of UiO-66, UiO-67 and their derivatives. Chem. Commun. *49*, 9449.

63. Schaate, A., Roy, P., Godt, A., Lippke, J., Waltz, F., Wiebcke, M., and Behrens, P. (2011). Modulated synthesis of Zr-based metal–organic frameworks: from nano to single crystals. Chem. Eur. J. *17*, 6643.

64. Wu, H., Chua, Y.S., Krungleviciute, V., Tyagi, M., Chen, P., Yildirim, T., and Zhou, W. (2013). Unusual and highly tunable missing-linker defects in zirconium metal–organic framework UiO-66 and their important effects on gas adsorption. J. Am. Chem. Soc. *135*, 10525.

65. Trickett, C.A., Gagnon, K.J., Lee, S., Gándara, F., Bürgi, H.-B., and Yaghi, O.M. (2015). Definitive molecular level characterization of defects in UiO-66 crystals. Angew. Chem. Int. Ed. *54*, 11162.

66. Goto, Y., Sato, H., Shinkai, S., and Sada, K. (2008). "Clickable" metal-organic framework. J. Am. Chem. Soc. *130*, 14354.

67. Shao, C., Wang, X., Zhang, Q., Luo, S., Zhao, J., and Hu, Y. (2011). Acid-base jointly promoted copper(I)-catalyzed azide-alkyne cycloaddition. J. Org. Chem. *76*, 6832.

68. Barrett, E.P., Joyner, L.G., and Halenda, P.P. (1951). The determination of pore volume and area distributions in porous substances. I. Computations from nitrogen isotherms. J. Am. Chem. Soc. *73*, 373.

69. Zahna, G., Schulze, H.A., Lippke, J., König, S., Sazamac, U., Fröba, M., and Behrens, P. (2015). A water-born Zr-based porous coordination polymer: modulated synthesis of Zr-fumarate MOF. Micropor. Mesopor. Mater *203*, 186.

70. Hirschle, P., Preiß, T., Auras, F., Pick, A., Völkner, J., Valdepérez, D., Witte, G., Parak, W.J., Rädler, J.O., and Wuttke, S. (2016). Exploration of MOF nanoparticle sizes using various physical characterization methods – is what you measure what you get? CrystEngComm *18*, 4359.

71. Perry, J.L., Reuter, K.G., Kai, M.P., Herlihy, K.P., Jones, S.W., Luft, J.C., Napier, M., Bear, J.E., and DeSimone, J.M. (2012). PEGylated PRINT nanoparticles: the impact of PEG density on protein binding, macrophage association, biodistribution, and pharmacokinetics. Nano Lett. *12*, 5304.

72. Gref, R., Domb, A., Quellec, P., Blunk, T., Müller, R.H., Verbavatz, J.M., and Langer, R. (2012). The controlled intravenous delivery of drugs using PEG-coated sterically stabilized nanospheres. Adv. Drug Deliv. Rev. *64*, 316.

73. Sebby, K.B., and Mansfield, E. (2015). Determination of the surface density of polyethylene glycol on gold nanoparticles by use of microscale thermogravimetric analysis. Anal. Bioanal. Chem. *407*, 2913.

74. Rouquerol, F., Rouquerol, J., and Sing, K. (1999). Adsorption by Powders and Porous Solids (Academic Press), p. p 219.

75. deKrafft, K.E., Boyle, W.S., Burk, L.M., Zhou, O.Z., and Lin, W. (2012). Zr- and Hf-based nanoscale metal–organic frameworks as contrast agents for computed tomography. J. Mater. Chem. *22*, 18139.

76. Sun, C.-Y., Qin, C., Wang, X.-L., Yang, G.-S., Shao, K.-Z., Lan, Y.-Q., Su, Z.-M., Huang, P., Wang, C.-G., and Wang, E.-B. (2012). Zeolitic imidazolate framework-8 as efficient pH-sensitive drug delivery vehicle. Dalton Trans. *41*, 6906.

77. Bellido, E., Guillevic, M., Hidalgo, T., Santander-Ortega, M.J., Serre, C., and Horcajada, P. (2014). Understanding the colloidal stability of the mesoporous MIL-100(Fe) nanoparticles in physiological media. Langmuir *30*, 5911.

78. Li, Z., and Zeng, H.C. (2014). Armored MOFs: enforcing soft microporous MOF nanocrystals with hard mesoporous silica. J. Am. Chem. Soc. *136*, 5631.

79. Huang, X., and Brazel, C.S. (2001). On the importance and mechanisms of burst release in matrix-controlled drug delivery systems. J. Control Release *73*, 121.

80. Javadi, M., Pitt, W.G., Tracy, C.M., Barrow, J.R., Willardson, B.M., Hartley, J.M., and Tsosie, N.H. (2013). Ultrasonic gene and drug delivery using eLiposomes. J. Control Release *167*, 92.

81. Deutsch, C., Taylor, J.S., and Wilson, D.F. (1982). Regulation of intracellular pH by human peripheral blood lymphocytes as measured by $^{19}F$ NMR. Proc. Natl. Acad. Sci. USA *79*, 7944.

82. Orellana-Tavra, C., Marshall, R.J., Baxter, E.F., Abánades Lázaro, I., Tao, A., Cheetham, A.K., Forgan, R.S., and Fairen-Jimenez, D. (2016). Drug delivery and controlled release from biocompatible metal–organic frameworks using mechanical amorphization. J. Mater. Chem. B *4*, 7697.

83. Mellman, I. (1996). Endocytosis and molecular sorting. Annu. Rev. Cell Dev. Biol. *12*, 575.

84. Rejman, J., Oberle, V., Zuhorn, I.S., and Hoekstra, D. (2004). Size-dependent internalization of particles via the pathways of clathrin- and caveolae-mediated endocytosis. Biochem. J. *377*, 159.

85. McMahon, H.T., and Boucrot, E. (2011). Molecular mechanism and physiological functions of clathrin-mediated endocytosis. Nat. Rev. Mol. Cell Biol. *12*, 517.

86. Mayor, S., and Pagano, R.E. (2007). Pathways of clathrin-independent endocytosis. Nat. Rev. Mol. Cell Biol. *8*, 603.

87. Gonzalez-Gaitan, M., and Stenmark, H. (2003). Endocytosis and signaling: a relationship under development. Cell *115*, 513.

88. Shin, J., and Abraham, S.N. (2001). Co-option of endocytic functions of cellular caveolae by pathogens. Immunology *102*, 2.

89. Tuthill, T.J., Groppelli, E., Hogle, J.M., and Rowlands, D.J. (2010). Picornaviruses. Curr. Top. Microbiol. Immunol. *343*, 43.

90. Vercauteren, D., Vandenbroucke, R.E., Jones, A.T., Rejman, J., Demeester, J., De Smedt, S.C., Sanders, N.N., and Braeckmans, K. (2010). The use of inhibitors to study endocytic pathways of gene carriers: optimization and pitfalls. Mol. Ther. *18*, 561.

91. Chen, Y., Wang, S., Lu, X., Zhang, H., Fu, Y., and Luo, Y. (2011). Cholesterol sequestration by nystatin enhances the uptake and activity of endostatin in endothelium via regulating distinct endocytic pathways. Blood *117*, 6392.

92. Hufnagel, H., Hakim, P., Lima, A., and Hollfelder, F. (2009). Fluid phase endocytosis contributes to transfection of DNA by PEI-25. Mol. Ther. *17*, 1411.

93. Sarkar, K., Kruhlak, M.J., Erlandsen, S.L., and Shaw, S. (2005). Selective inhibition by

rottlerin of macropinocytosis in monocyte-derived dendritic cells. Immunology *116*, 513.

94. Park, J., Jiang, Q., Feng, D., Mao, L., and Zhou, H.–C. (2016). Size-controlled synthesis of porphyrinic metal-organic framework and functionalization for targeted photodynamic therapy. J. Am. Chem. Soc. *138*, 3518.

95. Lim, J.P., and Gleeson, P.A. (2011). Macropinocytosis: an endocytic pathway for internalising large gulps. Immunol. Cell Biol. *89*, 836.

96. Michelakis, E.D., Webster, L., and Mackey, J.R. (2008). Dichloroacetate (DCA) as a potential metabolic-targeting therapy for cancer. Br. J. Cancer *99*, 989.

97. Bonnet, S., Archer, S.L., Allalunis-Turner, J., Haromy, A., Beaulieu, C., Thompson, R., Lee, C.T., Lopaschuk, G.D., Puttagunta, L., Bonnet, S., et al. (2007). A mitochondria-$K^+$ channel axis is suppressed in cancer and its normalization promotes apoptosis and inhibits cancer growth. Cancer Cell *11*, 37.

98. Badr, M.M., Qinna, N.A., Qadan, F., and Matalka, K.Z. (2014). Dichloroacetate modulates cytokines toward T helper 1 function via induction of the interleukin-12–interferon-γ pathway. Onco Targets Ther. *7*, 193.

99. Stacpoole, P.W., Nagaraja, N.V., and Hutson, A.D. (2003). Efficacy of dichloroacetate as a lactate-lowering drug. J. Clin. Pharmacol. *43*, 683.

100. Wang, W., Wang, L., Li, Y., Liu, S., Xie, Z., and Jing, X. (2016). Nanoscale polymer metal-organic framework hybrids for effective photothermal therapy of colon cancers. Adv. Mater. *28*, 9320.

101. Calik, M., Sick, T., Dogru, M., Döblinger, M., Datz, S., Budde, H., Hartschuh, A., Auras, F., and Bein, T. (2016). From highly crystalline to outer surface-functionalized covalent organic frameworks—a modulation approach. J. Am. Chem. Soc. *138*, 1234.